

# Charge order, nematicity and Mott insulating ground states in small-angle twisted bilayer graphene

Markus J. Klug<sup>1,\*</sup>

<sup>1</sup>*Institut für Theorie der Kondensierten Materie,  
Karlsruher Institut für Technologie, 76131 Karlsruhe, Germany*  
(Dated: December 16, 2019)

In this work, we determine states of electronic order of small-angle twisted bilayer graphene. Ground states are determined for weak- and strong-couplings being representatives for varying distance of the twist-angle from its magic value. In the weak-coupling regime, charge density waves emerge which break translational and  $C_3$ -rotational symmetry. In the strong coupling-regime, we find rotational and translational symmetry breaking Mott insulating states for all commensurate moiré band fillings. Depending on the local occupation of superlattice sites hosting up to four electrons, global spin-(ferromagnetic) and valley symmetries are also broken giving rise to characteristic Landau level degeneracies in detailed agreement with observations for commensurate band fillings of  $\nu = 0, \pm 1/2, \pm 3/4$ . The formation of those particular electron orders is traced back to the important role of characteristic non-local interactions which connect states sharing one hexagon of AB- and BA-stacked regions of the superlattice.

The temperature - gate voltage phase diagram of twisted bilayer graphene (TBG) in the small-angle regime is characterized by correlated insulator states as seen in transport experiments [1–5]. Their regular pattern of occurrences at commensurate fillings of the weakly dispersing moiré bands with bandwidths as small as 10meV [6] indicates an enhanced role of interaction effects, including strong-coupling Mott physics complemented by other complex electron phenomena such as superconductivity [1–5], linear-in-temperature resistivity [5], correlated electron states observed in STM and STS measurements [7–10], ferromagnetism and quantum hall physics [11]. Though vast theoretical efforts were made to model the electronic structure [12–19], as well as to explain the superconducting pairing mechanism [20–34] and the insulating states [15, 35–41], a comprehensive understanding of the insulating states for variable carrier concentrations is lacking. This is obviously important if one wants to identify the mechanism of superconductivity in these systems.

Quantum oscillations reveal that the insulating states differ in their Landau level degeneracy [1–4]. This indicates the presence (or absence) of (global) symmetries which generate Kramer-like degeneracies of single-particle states. In our description we assume the presence of spin-rotation and valley symmetry which is justified in the limit of vanishing spin-orbit coupling [42] and small twist-angles [15]. This implies for the insulator state at charge neutrality ( $\nu = 0$ ), which is found to be 4-fold degenerate, the presence of both spin- and valley-symmetry, for half electron- or hole-filling ( $\nu = \pm 1/2$ ) being two-fold degenerate that either spin- or valley-symmetry is broken, and for band filling  $\nu = \pm 3/4$  being single degenerate that both spin- and valley-symmetry are absent [2–4]. Those findings put strong requirements on possible

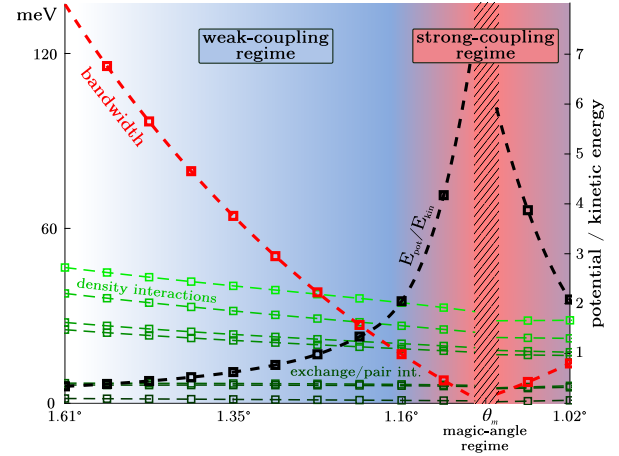


Figure 1. By tuning the twist-angle, twisted-bilayer graphene undergoes a transition from a weak into a strong-coupling regime. The moiré bandwidth (red) represents the kinetic energy scale, the amplitudes of interaction matrix elements of Eq. 4 (green) the potential energy scale. Their ratio (black) grows towards the magic-angle regime signaling the crossover.

ground states of insulating states.

In addition to transport experiments [1–5], which were performed on samples identified with the so-called *magic-angle regime* [6] hosting among others Mott-like insulator states and superconductivity, STS and STM experiments revealed correlated electron states for large doping ranges around charge neutrality (CN) [7–10]. Here interaction effects manifest themselves as significant redistribution of single-particle spectral weight setting in at certain electron- or hole-fillings of moiré bands. Additionally, it is unanimously reported that the correlated states break  $C_3$ -rotational symmetry as seen in spatially resolved charge distribution measurements and that the effect is largest at CN. Those results were obtained for samples with moiré bandwidths significantly larger than

\* markus.klug@kit.edu

10meV perhaps placing them in a *close-to-magic-angle regime*, where correlation effects are expected to be still present yet with interaction energies smaller than in the magic-angle regime. Notice, the role of interaction effects is in general not determined by the twist-angle alone. As the magic angle regime is determined by the dimensionless quantity  $\alpha = \frac{3}{8\pi} \frac{t_{\perp}}{\hbar v_F \sin \theta/2}$ , which takes on the value  $\alpha_m \approx 1/\sqrt{3}$  in the magic angle regime [6], the bandwidth of the single-particle spectrum and thus the role of interaction effects depend on the twist-angle  $\theta$ , the interlayer coupling  $t_{\perp}$  and the bare Fermi velocity  $v_F$ . A graphical depiction of the crossover from weak- to strong-coupling by tuning the twist-angle (or equally the interlayer coupling) is given in Fig. 1.

In this work, we investigate possible electronic ground states in the presence of finite-range Coulomb electron-electron interaction as function of doping. We will distinguish between two parameter regimes, a strong-coupling regime  $\alpha \approx \alpha_m$  representative for angles in the vicinity of the magic-angle where interaction effects dominate, and a weak-coupling regime  $|\alpha - \alpha_m| > 0$  where interaction effects are subleading. As outlined above, both regimes are likely to be realized in experiments.

In a first step, we set up a single-particle continuum theory for TBG as discussed in Refs. [6, 43], with superlattice translational  $T$ , crystalline point group  $D_6$ , spin  $SU(2)$ , and valley conservation  $U_v(1)$  approximate symmetries [16]. Interaction effects are considered by employing a two-orbital model introduced in Refs. [12, 13], where maximally localized Wannier orbitals centered at AB- and BA-stacked regions of the superlattice are constructed from the four moiré bands. Subsequently, interaction matrix elements between the Wannier states in the direct, exchange and pair-hopping channel are computed, which are found to be highly non-local.

In the *weak-coupling regime*, our results, which are obtained in an unrestricted mean field analysis, reveal a formation of stripe charge density wave order with commensurate ordering vectors of half of the reciprocal lat-

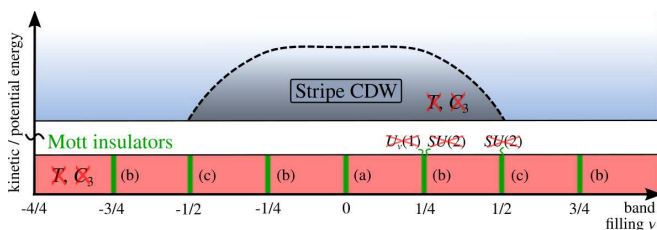


Figure 2. In the *weak-coupling regime*, our ground state analysis reveals a formation of stripe charge density wave orders which break translational  $T$  and  $C_3$ -rotational symmetries. In the *strong-coupling regime*, we find three types of Mott insulating ground states (a, b, c) for all commensurate moiré band fillings  $\nu = 0, \pm 1/4, \pm 1/2, \pm 3/4$ , which resemble the stripe-type orders in the weak-coupling limit (a) but differ, in part, by the absence of spin  $SU(2)$  (b) as well as valley  $U_v(1)$  symmetry (c).

tice vectors of the moiré superlattice. The charge inhomogeneities form when the interaction strength and the moiré band filling reaches a certain threshold. However, we find no indication for an instability linked to the van-Hove singularities of the single-particle spectrum.

In the *strong-coupling regime*, we perform an infinite coupling limit where we drop the kinetic part of the theory and consider only interaction processes which can be expressed in terms of density-density interactions. This approach would be futile in the limit of local Hubbard interactions. However, for the present model, the important role of non-locality combined with ferromagnetic and ferrovalley exchange interactions distinguishing between spin and valley number allows us to determine the nature of ordered states even without kinetic energy contributions of electrons. For all commensurate band fillings  $\nu = 0, \pm 1/4, \pm 1/2, \pm 3/4$ , we find Mott insulating ground states which break translational  $T$  and rotational  $C_3$  symmetry ( $\nu = 0$ ), as well as spin  $SU(2)$  symmetry ( $\nu = \pm 1/4, \pm 1/2, \pm 3/4$ ) and valley  $U_v(1)$  symmetry ( $\nu = \pm 1/4, \pm 3/4$ ), see Fig. 2.

## I. MICROSCOPIC MODEL

We first obtain the weakly dispersing moiré bands by considering a continuum model [6, 43] where states near the slightly twisted Dirac cones of two graphene layers hybridize due to a finite inter-layer coupling. Because of the large separation in momentum space, states near non-equivalent cones, in the following labeled by the valley quantum number  $\xi = \pm$ , are assumed to be effectively decoupled generating an emergent  $U_v(1)$  valley symmetry.

The single-particle Hamiltonian for TBG expressed in the graphene basis  $\phi_{\mathbf{K}\xi\sigma}$  is written as [43]

$$H_{TBG} = \sum_{\mathbf{K}\sigma\xi} \phi_{\mathbf{K}\xi\sigma}^\dagger \begin{pmatrix} H_{\xi,\theta/2} - \mu & T \\ T^\dagger & H_{\xi,-\theta/2} - \mu \end{pmatrix} \phi_{\mathbf{K}\xi\sigma}, \quad (1)$$

where  $H_{\xi,\varphi}$  denotes the Hamiltonian of electrons in single layer graphene near valley  $\xi$  which is rotated by angle  $\varphi$ . Interlayer coupling is described by  $T$ . As parameters we choose the Fermi velocity to  $v_F \hbar/a = 2.1354\text{eV}$  and the inter-layer tunneling amplitudes, which discriminate between intra- and inter-sublattice processes, to  $t_{AA} = t_{BB} = 79.7\text{meV}$  and  $t_{AB} = 97.5\text{meV}$ , to take lattice relaxation effects into account following Ref. [13].  $\mathbf{K}$  denotes the crystal momentum in the single layer graphene Brillouin zone and  $\sigma$  the electron spin. Subsequently, the effective moiré Hamiltonian is obtained by considering only the four narrow bands around charge neutrality with dispersion relation  $\epsilon_{\lambda\mathbf{k}\xi}$  yielding

$$H_M = \sum_{\lambda\mathbf{k}\sigma\xi} (\epsilon_{\lambda\mathbf{k}\xi} - \mu) \psi_{\lambda\mathbf{k}\xi\sigma}^\dagger \psi_{\lambda\mathbf{k}\xi\sigma}, \quad (2)$$

where band index  $\lambda$ , spin  $\sigma$ , valley  $\xi$  and crystal momentum  $\mathbf{k}$ , element of the moiré Brillouin zone, label the superlattice Bloch states  $\psi_{\lambda\mathbf{k}\sigma\xi}$ .

### A. Construction of Wannier basis

The Wannier basis is constructed by employing a two-orbital model [13–15] where localized Wannier functions, though centered at the AB- and BA-stacked regions, possess highest weight at the AA-stacked regions of the underlying TBG superlattice. Despite the occurrence of Wannier obstructions, which render certain exact symmetries non-local [15, 16] and are resolved by incorporating auxiliary bands [17, 18] adding a vast number of degrees of freedom, we assume that the relevant physics of our work is captured by the two-orbital model. This assumption is further supported by the fact that topological properties are irrelevant when we discuss the limit of strong couplings where the electronic band structure is fully neglected. Furthermore, it holds also in the limit of weak couplings as only direct interaction matrix elements are found relevant for the weak-coupling analysis which do not depend on the phase of the single-particle states. In particular, we follow the approach outlined in Ref. [13] and construct orbitals centered at the AB- and BA-stacked regions having definite valley number by employing the method of maximally localized orbitals [44, 45]. Details about our construction of the Wannier basis are found in the Appendix A. Eventually, we obtain orthogonal and exponentially localized Wannier orbitals  $\Psi_{a\sigma}(\mathbf{r})$ , which are labeled by the single-particle quantum numbers  $a = (i, \alpha, \xi)$  and spin  $\sigma$  located in superlattice unit cell  $i$  and centered at the  $\alpha = \text{AB, BA}$ -stacked regions. This gives rise to 8 states per superlattice unit cell. The effective tight-binding model is given by

$$H = \sum_{ab\sigma} (t_{ab} - \mu\delta_{ab}) c_{a\sigma}^\dagger c_{b\sigma} + \frac{1}{2} \sum_{\sigma\sigma'} \sum_{abcd} U_{abcd} c_{a\sigma}^\dagger c_{b\sigma'}^\dagger c_{c\sigma'} c_{d\sigma}, \quad (3)$$

where the transition amplitudes  $t_{ab}$  are, by construction, diagonal in valley number and obtained by projecting the Bloch states into the Wannier basis.

### B. Interaction matrix elements

We compute the interaction matrix elements entering the effective Hamiltonian Eq. (3) between Wannier states by using an unscreened Coulomb kernel,

$$U_{abcd} = \frac{e^2}{4\pi\epsilon} \int_{\mathbf{r}\mathbf{r}'} \frac{\Psi_{a\sigma}^\dagger(\mathbf{r}) \Psi_{b\sigma'}^\dagger(\mathbf{r}') \Psi_{c\sigma'}(\mathbf{r}') \Psi_{d\sigma}(\mathbf{r})}{|\mathbf{r} - \mathbf{r}'|}, \quad (4)$$

with electron charge  $e$  and relative permittivity  $\epsilon \approx 7$  for hexagonal boron nitride. We distinguish between density ( $a = d$  and  $b = c$  introducing  $U = U_{abba}$ ), exchange ( $a = c \neq b = d$  introducing  $J = U_{abab}$ ), and pair-hopping ( $a = b \neq c = d$  introducing  $X = U_{aabb}$ ). We also checked for charge-bond interaction matrix elements ( $a \neq d \neq b = c$ ), but find them at least one order

of magnitude smaller than comparable processes and are therefore safely neglected. Generally, we distinguish between intra-valley processes, where the valley indices in  $a$  and  $b$  are identical, and inter-valley processes, where the valley indices in  $a$  and  $b$  differ. The latter are labeled by the subscript  $IV$  in the following.

We find that the amplitude of interaction matrix elements drops with distance but remains significant for processes connecting all orbitals which share one hexagon formed by AB- and BA-stacked regions of the superlattice, as depicted in Fig. 3. In general, interactions are dominated by direct interaction processes. Since this type of interaction is insensitive to local valley or spin configurations, we expect that possible charge modulations are determined by  $U$ . Though at least one order smaller in amplitude but being sensitive to valley and spin number, intra- and inter-valley exchange  $J$  and  $J_{IV}$ , as well as intra- and inter-valley pair-hopping  $X$  and  $X_{IV}$  processes are expected to be relevant. Due to rapid phase fluctuations, inter-valley processes are much smaller. However, because of the coupling of otherwise decoupled valley sectors, they are considered relevant to determine the exact ground state. For both the intra- and inter-valley case, all matrix elements are found positive  $J, J_{IV} > 0$  causing neighboring spin- and orbital-degrees of freedom to align. Concluding, the hierarchy of amplitudes of interaction matrix elements,

$$U \gg J > |X| \gg J_{IV} > |X_{IV}|, \quad (5)$$

is characteristic for small-angle TBG.

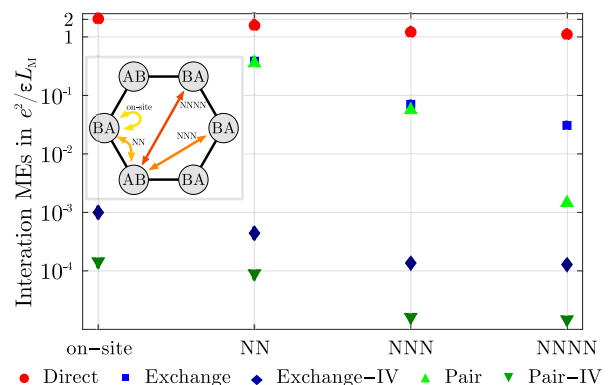


Figure 3. Amplitudes of interaction matrix elements in units of  $e^2/\epsilon L_M$  with the superlattice length scale  $L_M = \frac{a}{2 \sin \theta/2}$  for  $\theta = 1.05^\circ$ . All interactions connecting sites which share one hexagon are found to be relevant. Longer-distance interactions are numerically small and are therefore negligible. Since the twist-angle dependence of interaction matrix element is rather weak and approximately determined by the superlattice length scale  $U_{abcd} \propto L_M^{-1} \propto \sin(\theta/2)$  as depicted in Fig. 1 and being complementary to Ref. [19], the numerical values are representative for both the strong- and weak-coupling regime.

## II. GROUND STATE ANALYSIS

The effective two-orbital model Eq. (3) established in the previous sections constitutes the basis for the subsequent ground state analysis, which is two-fold: We first investigate the weak-coupling regime for  $|\alpha - \alpha_m| > 0$ , and second, conduct a strong coupling analysis for  $\alpha \approx \alpha_m$ . It is noted that the following ground state analysis does not depend on the actual twist-angle or the inter-layer transition amplitude as tuning the twist-angle causes (to leading order) quantitative but no qualitative changes to the electronic band structure and interaction matrix elements.

### A. Weak-coupling regime

For small coupling strength, we conduct a mean field analysis in which interaction terms are locally decoupled in all possible channels,

$$\begin{aligned} c_{a\sigma}^\dagger c_{b\sigma'}^\dagger c_{c\sigma'} c_{d\sigma} &\approx \langle c_{b\sigma'}^\dagger c_{c\sigma'} \rangle c_{a\sigma}^\dagger c_{d\sigma} + \langle c_{a\sigma}^\dagger c_{d\sigma} \rangle c_{b\sigma'}^\dagger c_{c\sigma'} \\ &- \langle c_{a\sigma}^\dagger c_{c\sigma'} \rangle c_{b\sigma'}^\dagger c_{d\sigma} - \langle c_{a\sigma}^\dagger c_{c\sigma'} \rangle c_{b\sigma'}^\dagger c_{d\sigma} + \text{const..} \end{aligned} \quad (6)$$

This ensures that our analysis is susceptible to various kinds of electron instabilities. The ground state is eventually determined by minimizing an energy functional where mean fields are considered as variational parameters on a finite lattice of  $30 \times 30$  superlattice unit cells. Details to the numerical computation scheme are found in the Appendix B.

For a large amount of electron- or hole-doping, we find no electronic order (recall, we do not probe for superconductivity) and the characteristic van-Hove singularities as well as the linear dispersion relation near charge neutrality in the density of states are observed as depicted in Fig. 4.

In contrast, for moderate electron- or hole-doping, we observe the formation of a stripe charge density wave order which breaks translational and rotational  $C_3$ -symmetry. Here, the local electron density is parametrized by

$$\langle \hat{n}_{a\sigma} \rangle = n + \Delta_{\mathbf{Q}} \cos(\mathbf{Q} \cdot \mathbf{R}_a), \quad (7)$$

where the order parameter is given by

$$\Delta_{\mathbf{Q}} = \sum_{\mathbf{k}\alpha\xi\sigma} \langle c_{\mathbf{k}+\mathbf{Q}\alpha\xi\sigma}^\dagger c_{\mathbf{k}\alpha\xi\sigma} \rangle, \quad (8)$$

with the electron density  $n = \frac{1}{N} \sum_{a\sigma} \langle \hat{n}_{a\sigma} \rangle$ , the particle number operator  $\hat{n}_{a\sigma} = c_{a\sigma}^\dagger c_{a\sigma}$  and lattice site vector  $\mathbf{R}_a$ . Possible ordering vectors are  $\mathbf{Q} \in \{\mathbf{G}_1/2, \mathbf{G}_2/2, (\mathbf{G}_1 + \mathbf{G}_2)/2\}$  with  $\mathbf{G}_i$  reciprocal superlattice vectors. Its onset is determined by a critical concentration of electrons or holes signaled by a significant distortion of the single-particle spectrum as depicted Fig. 4. When tuning towards the magic-angle, the lower (upper)

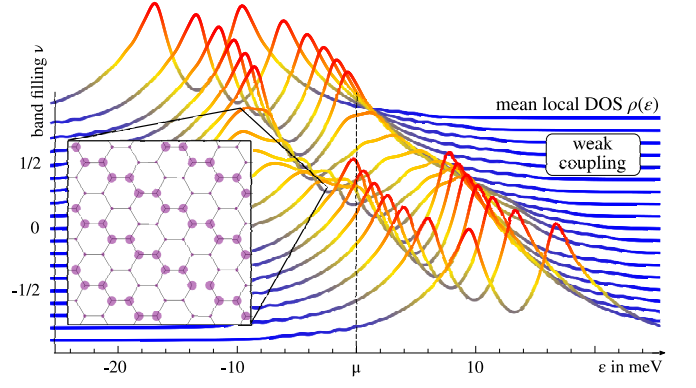


Figure 4. Mean local density of states as function of frequency ( $x$ -axis) for various moiré band fillings ( $y$ -axis) for a fixed twist-angle in the *weak-coupling regime*. The local density of states is averaged over all lattice site and given by  $\rho(\epsilon) = -\frac{1}{\pi N} \sum_{a,\sigma} \text{Im} G_{aa,\sigma\sigma}^R(\epsilon)$ , where the retarded Green's function is obtained from the mean field Hamiltonian as given in Eq. B3 and  $N$  denotes the number of lattice sites. In the normal state, the single-particle spectrum is characterized by van-Hove peaks as observable for high and low densities. The onset of a stripe density wave order causes a significant distortion of the single-particle spectrum, where the effect is largest around half filling. A possible real space representation of the order with  $\Delta_{\mathbf{Q}}/n \approx 0.126$  is depicted in the inlet where the hexagon's vertices represent the AB- and BA-stacked regions of the superlattice. The purple dot's diameter scales with the local occupation of orbitals  $\bullet \propto \sum_{\xi\sigma} \langle \hat{n}_{i\alpha\xi\sigma} \rangle$ .

critical band filling decreases (increases) and the parameter regime of the stripe charge density wave order increases, as depicted in Fig. 2, due to decreasing kinetic energy contributions.

The observations are understood by setting up a corresponding mean field theory which is presented in Appendix C. As charge modulations are predominantly determined by direct interaction processes with numerically large interaction matrix elements, exchange and pair-hopping processes are here neglected and the effective interaction in the corresponding channel is determined to

$$U_{\text{CDW}} = U_{\text{on-site}} + U_{\text{NN}} - 4U_{\text{NNN}} - 3U_{\text{NNNN}}, \quad (9)$$

which may be negative for sufficiently large  $U_{\text{NNN}}$ ,  $U_{\text{NNNN}}$  and small  $U_{\text{on-site}}$ ,  $U_{\text{NN}}$  interaction matrix elements. This is made plausible by inspecting a possible real space representation of the charge density wave order depicted in the inlet of Fig. 4: On mean field level, this charge configuration minimizes interaction contributions from NNN and NNNN direct interaction processes. In particular for the numerical values of interaction matrix elements determined in Sec. IB,  $U_{\text{CDW}}/U_{\text{on-site}} \approx -2, 2$  and the effective interaction is attractive. This finding is complemented by results for the static charge susceptibility with finite momentum transfer. It is peaked for doping levels around charge neutrality with small peaks at the van Hove point, but does not diverge due to the

absence of nesting conditions (see Appendix C for details). An onset of this order therefore requires a finite, attractive interaction strength and follows the qualitative illustration depicted in Fig. 2.

A possible real space realization of the stripe density charge order is depicted in the inset of Fig. 4. It is noted that the corresponding real-space charge distribution, accessible e.g. in STM measurements, differs qualitatively because of the highly non-local shape of Wannier orbitals with highest localization probability at the hexagon's centers. The local charge distribution would rather resemble a distorted version of the disordered state breaking rotational-C3 symmetry.

### B. Strong-coupling regime

In the magic-angle regime, kinetic energy contributions of electrons are expected to be much smaller than contribution from interaction processes (see Fig. 1). We therefore consider *density-density interaction* processes only. This approximation renders the local occupation number a good quantum number and the theory integrable. Later, kinetic contribution may be incorporated perturbatively in orders of  $\sim t/U$ , which is however not part of this work. In this limit of infinite coupling, the Hamiltonian contains only contributions from direct and exchange interaction processes,

$$H_{SC} = \frac{1}{2} \sum_{\sigma\sigma'} \sum_{ab \in \square} (U_{ab} - J_{ab} \delta_{\sigma\sigma'}) (\hat{n}_{a\sigma} - \frac{1}{2}) (\hat{n}_{b\sigma'} - \frac{1}{2}), \quad (10)$$

where  $\hat{n}_{\alpha\sigma}$  represents the local occupation number operator. This model is particle-hole symmetric, i.e. invariant under  $\hat{n}_{\alpha\sigma} \rightarrow 1 - \hat{n}_{\alpha\sigma}$ , which allows us to study either hole or electron doping. Since electronic single-particle states are either occupied or empty,  $\langle \hat{n}_{\alpha\sigma} \rangle = 0, 1$ , the ground state is determined by minimizing the energy functional  $E[\langle n \rangle] = \langle H_{SC} \rangle$  with local occupation numbers as variational parameters. The optimization problem is solved using the conventional Monte Carlo based simulated-annealing-algorithm [46].

For all commensurate moiré band fillings  $\nu = 0, \pm 1/4, \pm 1/2, \pm 3/4$  we find Mott-insulating ground states. When adding or removing electrons we expect that the insulator turns into a conductor where single particles move in a landscape of potential barriers generated by electrons and holes constituting the nearest Mott insulating state. Our results of possible ground states of the hole-doped side are depicted in Fig. 5.

For moiré band fillings  $\nu = 0, \pm 1/4$ , we observe stripe-type orders which resemble our findings of the the weak-coupling approach with charge inhomogeneities are described by ordering vectors as given in Eq. (8). It indicates, that this particular density configuration minimizes the potential energy costs generated by the dominant direct interaction processes irrespective of kinetic

energy contributions. It supports our earlier presumption that the formation of density inhomogeneities in the weak coupling-regime is not linked to features of the single-particle spectrum (e.g. nesting). For  $\nu = \pm 1/2, \pm 3/4$ , we find charge configurations which maximize the distance between charges similar to the principal of Wigner crystallization.

We conclude that the charge distribution is decisively determined by direct interaction processes  $U$  which are characterized by a significant coupling of all sites sharing one hexagon. It is determined solely by the ratio of direct interaction terms, which was determined to  $(U_{\text{on-site}} : U_{\text{NN}} : U_{\text{NNN}} : U_{\text{NNNN}}) / U_{\text{on-site}} = (1 : 0.79 : 0.63 : 0.58)$ , where the exact numerical values matter (i.e. simple ratios of type  $(1 : \frac{2}{3} : \frac{2}{3} : \frac{1}{3})$  being suggestive when counting the direct overlap of wannier orbitals lead to qualitatively different results). Furthermore, since the local single-particle states are either empty or occupied, the particular ground state is required, unless occupied lattice sites are always fully occupied, to additionally break the spin- and / or valley-symmetry. Since direct interaction processes do not discriminate between spin and charge degrees-of-freedom, the energetically most favorable configuration is here determined by exchange interactions. Their matrix elements, for both the intra- and inter-valley channel, are always found to be positive and therefore favor an alignment of spins non-locally (because of intra-valley exchange) and locally (because of inter-valley

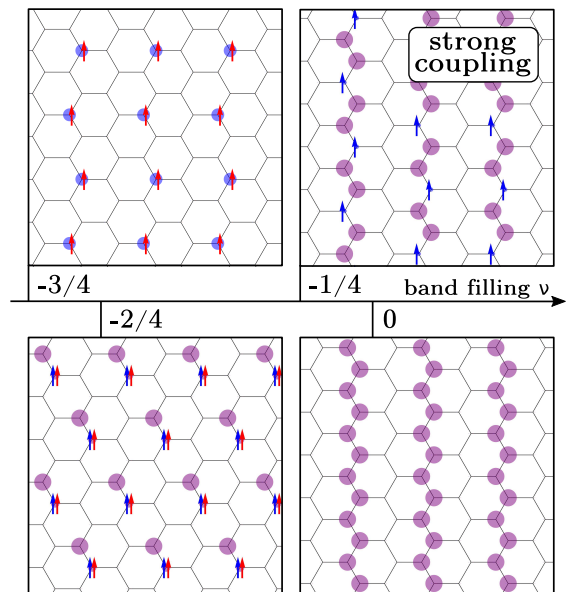


Figure 5. Real-space representations of possible ground states in the *strong-coupling regime* which exhibit Mott insulating behavior. The occupation number at one particular lattice site, which hosts in total 4 electronic states, is symbolically indicated as follows (arrows represent spin up / down state, color red / blue valley  $\xi = \pm 1$  state): 4/4 occupation  $\bullet$ , 3/4 occupation  $\uparrow \downarrow$ , 1/2 occupation  $\uparrow \downarrow$ , 1/4 occupation  $\uparrow$  or  $\downarrow$ , else empty.

exchange). This results for  $\nu = \pm 1/4, \pm 3/4$  in a condensation of local degrees of freedom of partially occupied sites in one particular spin and valley sector, whereas for  $\nu = \pm 1/2$  in one particular spin sector because on-site intra-valley exchange interaction is absent, as depicted in Fig. 5. These findings are in agreement with the experimental observations outlined above.

### III. CONCLUSION

We found a hierarchy of interaction processes, Eq. (5), where direct interaction processes between states sharing one hexagon dominate, followed by intra- and inter-valley exchange interaction processes which are at least one order in magnitude smaller but always positive. Combined with a matrix elements' dependence on distance, those characteristic were found decisive for the analysis of possible electronic ground states. Our findings have to be contrasted to a similar strong coupling approach presented in Ref. [39] where the authors assumed an averaged interaction strength for all processes connecting states sharing one hexagon and also included processes beyond the density channel. As our results depend decisively on the distance dependence of interaction elements, our ground states for commensurate fillings  $\nu = \pm 1/2, \pm 3/4$  differ from those determined in Ref. [39].

The most robust finding of our analysis, that occurs at weak and strong coupling, is the emergence of a nematic

state that breaks the three-fold rotation symmetry of the moiré lattice. The details of the related translational symmetry breaking and of additional broken symmetries depend then on the strength of the interaction and the filling fractions. While critical fluctuations, not included in our formalism, may render charge density waves, spin, or valley order finite ranged, the discrete nematic symmetry breaking should give rise to a sharp second-order phase transition with a finite transition temperature. Even for moderate symmetry-breaking substrate-induced strain we expect a well defined crossover temperature.

In addition to the nematic state, we find an onset of spin- and valley-polarized orders at strong coupling. This effect is due to the non-local, positive intra-valley and inter-valley exchange couplings suggesting modified Hund's rule, where first the spin and subsequently the valley number is maximized when filling up superlattice sites with electrons. This yields the observed degeneracy pattern of the observed insulating states.

If the nematic order exist away from incommensurate filling the reduced symmetry at  $T_c$  exclude more complex superconducting order parameters, such as chiral  $d+id$  or nematic  $d+id$  states. On the other hand, the abundance of nematic order in twisted bilayer suggests that nematic fluctuations may be important in inducing or amplifying superconductivity in these materials [29, 47, 48].

*Acknowledgements:* We thank B. Anderson, R. Fernandes, J. Kang, L. Merckens, J. Schmalian and A. Wechselberger for insightful discussions.

- 
- [1] Y. Cao, V. Fatemi, A. Demir, S. Fang, S. L. Tomarken, J. Y. Luo, J. D. Sanchez-Yamagishi, K. Watanabe, T. Taniguchi, E. Kaxiras, R. C. Ashoori, and P. Jarillo-Herrero, *Nature* **556**, 80 (2018).
- [2] Y. Cao, V. Fatemi, S. Fang, K. Watanabe, T. Taniguchi, E. Kaxiras, and P. Jarillo-Herrero, *Nature* **556**, 43 (2018).
- [3] M. Yankowitz, S. Chen, H. Polshyn, Y. Zhang, K. Watanabe, T. Taniguchi, D. Graf, A. F. Young, and C. R. Dean, *Science* **363**, 1059 (2019).
- [4] X. Lu, P. Stepanov, W. Yang, M. Xie, M. A. Aamir, I. Das, C. Urgell, K. Watanabe, T. Taniguchi, G. Zhang, A. Bachtold, A. H. MacDonald, and D. K. Efetov, arXiv e-prints, arXiv:1903.06513 (2019), arXiv:1903.06513 [cond-mat.str-el].
- [5] H. Polshyn, M. Yankowitz, S. Chen, Y. Zhang, K. Watanabe, T. Taniguchi, C. R. Dean, and A. F. Young, *Nat. Phys.* (2019), 10.1038/s41567-019-0596-3.
- [6] R. Bistritzer and A. H. MacDonald, *Proc. Natl. Acad. Sci.* **108**, 12233 (2011).
- [7] A. Kerelsky, L. J. McGilly, D. M. Kennes, L. Xian, M. Yankowitz, S. Chen, K. Watanabe, T. Taniguchi, J. Hone, C. Dean, A. Rubio, and A. N. Pasupathy, *Nature* **572**, 95 (2019).
- [8] Y. Choi, J. Kemmer, Y. Peng, A. Thomson, H. Arora, R. Polski, Y. Zhang, H. Ren, J. Alicea, G. Refael, F. von Oppen, K. Watanabe, T. Taniguchi, and S. Nadj-Perge, *Nature* (2019), 10.1038/s41567-019-0606-5.
- [9] Y. Jiang, X. Lai, K. Watanabe, T. Taniguchi, K. Haule, J. Mao, and E. Y. Andrei, *Nature* (2019), 10.1038/s41586-019-1460-4.
- [10] Y. Xie, B. Lian, B. Jäck, X. Liu, C.-L. Chiu, K. Watanabe, T. Taniguchi, B. A. Bernevig, and A. Yazdani, *Nature* **572**, 101 (2019).
- [11] A. L. Sharpe, E. J. Fox, A. W. Barnard, J. Finney, K. Watanabe, T. Taniguchi, M. A. Kastner, and D. Goldhaber-Gordon, *Science* **365**, 605 (2019).
- [12] N. F. Q. Yuan and L. Fu, *Phys. Rev. B* **98**, 045103 (2018).
- [13] M. Koshino, N. F. Q. Yuan, T. Koretsune, M. Ochi, K. Kuroki, and L. Fu, *Phys. Rev. X* **8**, 031087 (2018).
- [14] J. Kang and O. Vafek, *Phys. Rev. X* **8**, 031088 (2018).
- [15] H. C. Po, L. Zou, A. Vishwanath, and T. Senthil, *Phys. Rev. X* **8**, 031089 (2018).
- [16] L. Zou, H. C. Po, A. Vishwanath, and T. Senthil, *Phys. Rev. B* **98**, 085435 (2018).
- [17] S. Carr, S. Fang, Z. Zhu, and E. Kaxiras, arXiv e-prints, arXiv:1901.03420 (2019), arXiv:1901.03420 [cond-mat.mes-hall].
- [18] H. C. Po, L. Zou, T. Senthil, and A. Vishwanath, *Phys. Rev. B* **99**, 195455 (2019).
- [19] Z. A. H. Goodwin, F. Corsetti, A. A. Mostofi, and J. Lischner, arXiv e-prints, arXiv:1905.01887 (2019), 1905.01887 [cond-mat.str-el].
- [20] E. Laksono, J. N. Leaw, A. Reaves, M. Singh, X. Wang, S. Adam, and X. Gu,

- Solid State Communications* **282**, 38 (2018).
- [21] C.-C. Liu, L.-D. Zhang, W.-Q. Chen, and F. Yang, *Phys. Rev. Lett.* **121**, 217001 (2018).
- [22] H. Guo, X. Zhu, S. Feng, and R. T. Scalettar, *Phys. Rev. B* **97**, 235453 (2018).
- [23] C. Xu and L. Balents, *Phys. Rev. Lett.* **121**, 087001 (2018).
- [24] A. Thomson, S. Chatterjee, S. Sachdev, and M. S. Scheurer, *Phys. Rev. B* **98**, 075109 (2018).
- [25] F. Wu, A. H. MacDonald, and I. Martin, *Phys. Rev. Lett.* **121**, 257001 (2018).
- [26] T. Huang, L. Zhang, and T. Ma, *Science Bulletin* **64**, 310 (2019).
- [27] T. J. Peltonen, R. Ojajärvi, and T. T. Heikkilä, *Phys. Rev. B* **98**, 220504(R) (2018).
- [28] D. M. Kennes, J. Lischner, and C. Karrasch, *Phys. Rev. B* **98**, 241407(R) (2018).
- [29] V. Kozii, H. Isobe, J. W. F. Venderbos, and L. Fu, *Phys. Rev. B* **99**, 144507 (2019).
- [30] B. Roy and V. Juričić, *Phys. Rev. B* **99**, 121407(R) (2019).
- [31] J. González and T. Stauber, *Phys. Rev. Lett.* **122**, 026801 (2019).
- [32] Y.-Z. You and A. Vishwanath, *npj Quantum Materials* **4**, 16 (2019).
- [33] M. S. Scheurer, R. Samajdar, and S. Sachdev, arXiv e-prints, arXiv:1906.03258 (2019), arXiv:1906.03258 [cond-mat.supr-con].
- [34] B. Lian, Z. Wang, and B. A. Bernevig, *Phys. Rev. Lett.* **122**, 257002 (2019).
- [35] H. Isobe, N. F. Q. Yuan, and L. Fu, *Phys. Rev. X* **8**, 041041 (2018).
- [36] J. F. Dodaro, S. A. Kivelson, Y. Schattner, X. Q. Sun, and C. Wang, *Phys. Rev. B* **98**, 075154 (2018).
- [37] M. Ochi, M. Koshino, and K. Kuroki, *Phys. Rev. B* **98**, 081102(R) (2018).
- [38] J. W. F. Venderbos and R. M. Fernandes, *Phys. Rev. B* **98**, 245103 (2018).
- [39] J. Kang and O. Vafek, *Phys. Rev. Lett.* **122**, 246401 (2019).
- [40] K. Seo, V. N. Kotov, and B. Uchoa, *Phys. Rev. Lett.* **122**, 246402 (2019).
- [41] L. Rademaker and P. Mellado, *Phys. Rev. B* **98**, 235158 (2018).
- [42] A. H. Castro Neto, F. Guinea, N. M. R. Peres, K. S. Novoselov, and A. K. Geim, *Rev. Mod. Phys.* **81**, 109 (2009).
- [43] D. Weckbecker, S. Shallcross, M. Fleischmann, N. Ray, S. Sharma, and O. Pankratov, *Phys. Rev. B* **93**, 035452 (2016).
- [44] N. Marzari and D. Vanderbilt, *Phys. Rev. B* **56**, 12847 (1997).
- [45] N. Marzari, A. A. Mostofi, J. R. Yates, I. Souza, and D. Vanderbilt, *Rev. Mod. Phys.* **84**, 1419 (2012).
- [46] S. Kirkpatrick, C. D. Gelatt, and M. P. Vecchi, *Science* **220**, 671 (1983).
- [47] S. Lederer, Y. Schattner, E. Berg, and S. A. Kivelson, *Phys. Rev. Lett.* **114**, 097001 (2015).
- [48] S. Lederer, Y. Schattner, E. Berg, and S. A. Kivelson, *Proc. Natl. Acad. Sci.* (2017), 10.1073/pnas.1620651114.
- [49] C. Lanczos, *J. Res. Natl. Bur. Stand. B* **45**, 255 (1950).
- [50] G. H. Golub and C. F. Van Loan, *Matrix Computations (4th Ed.)* (Johns Hopkins University Press, 2013).
- [51] P. Fazekas, *Lecture Notes on Electron Correlation and Magnetism* (World Scientific, 1999).

## Appendix A: Construction of maximally localized Wannier basis

The Wannier basis is constructed following the method of maximally localized Wannier functions [44, 45]. In the case of twisted bilayer graphene, we follow the approach presented in Ref. [13] where valley degrees of freedom are assumed to fully decouple in the limit of small twist-angles. We expect this approach to be equivalent to other two-orbital approaches [14, 15] which drop the requirements for a valley symmetry at first hand, but recover an approximate valley symmetry later. As the constructed orbital states possess a definite valley number, we drop the valley  $\xi$  and spin  $\sigma$  quantum numbers from the subsequent analysis.

Represented in spatial space, the Bloch functions introduced in Eq. 2 are

$$\psi_{\lambda\mathbf{k}}(\mathbf{r}) = \psi_{\lambda\mathbf{k}}^{(1,A)}(\mathbf{r}) + \psi_{\lambda\mathbf{k}}^{(1,B)}(\mathbf{r}) + \psi_{\lambda\mathbf{k}}^{(2,A)}(\mathbf{r}) + \psi_{\lambda\mathbf{k}}^{(2,B)}(\mathbf{r}), \quad (\text{A1})$$

where their projection on single-layer graphene (SLG) layer  $j = 1, 2$  and sublattice  $\gamma = A, B$  is given by

$$\psi_{\lambda\mathbf{k}}^{(j,\gamma)}(\mathbf{r}) = N^{-1/2} \sum_{im} U_{jmA}^{(\lambda)}(\mathbf{k}) e^{i(\mathbf{k} + \mathbf{G}_m)\mathbf{a}_i^{(j)}} \phi(\mathbf{r} - \mathbf{a}_i^{(j)} - \mathbf{u}_\gamma^{(j)}), \quad (\text{A2})$$

with reciprocal superlattice vector  $\mathbf{G}_m$ , SLG lattice vector  $\mathbf{a}_i^{(j)}$ , SLG basis vector  $\mathbf{u}_\gamma^{(j)}$ .  $\phi(\mathbf{r})$  represents SLG  $p_z$ -orbitals localized at  $\mathbf{r} = 0$ . The matrix  $U_{jmA}^{(\lambda)}$  connects the microscopic two-layer graphene tight-binding basis Eq. (1) to the moiré Bloch basis Eq. (2). Eventually, the Wannier function located in superlattice unit cell  $i$  centered at the  $\alpha = \text{AB, BA}$ -stacked region is obtained as superposition of Bloch functions [44, 45],

$$\Psi_{i\alpha}(\mathbf{r}) = N_{SL}^{-1/2} \sum_{\lambda\mathbf{k}} e^{-i\mathbf{k}\mathbf{A}_i} \mathcal{U}_{\lambda\mathbf{k}}^{(\alpha)} \Psi_{\lambda\mathbf{k}}(\mathbf{r}). \quad (\text{A3})$$

where the superlattice vector  $\mathbf{A}_i$ . The unitary matrix  $\mathcal{U}_{\lambda\mathbf{k}}^{(\alpha)}$  is chosen such that the spread functional

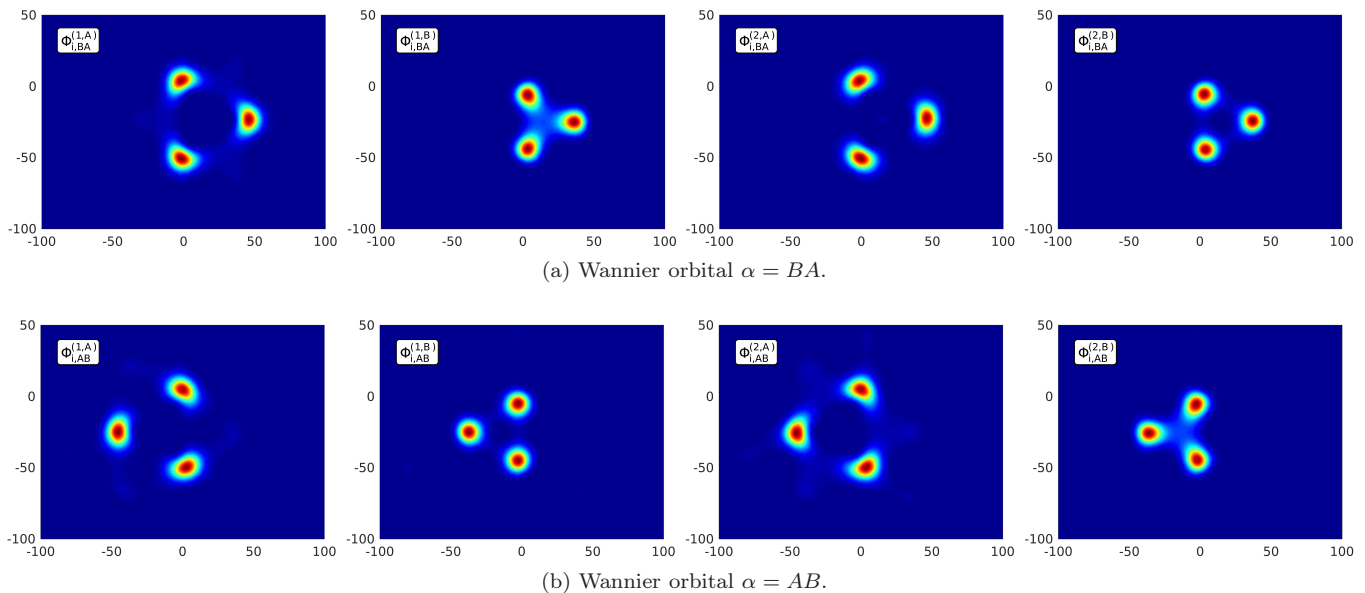


Figure 6. Constructed Wannier orbitals  $\Psi_{i\alpha}$  for  $\theta = 1.05^\circ$  projected on single-layer graphene sites labeled by lattice index  $j = 1, 2$  and sublattice index  $\gamma = A, B$ . The orbitals are centered at BA- and AB-stacked regions of the moiré superlattice and are exponentially localized.

$$g[\mathcal{U}] = \int d^d r \Psi_{i\alpha}^*(\mathbf{r}) (\mathbf{r} - \mathbf{r}_{i\alpha})^2 \Psi_{i\alpha}(\mathbf{r}) \quad (\text{A4})$$

is minimized. Here,  $\mathbf{r}_{i\alpha}$  represents the coordinates of the Wannier orbital's center located at the center of the AB- or BA-stacked regions of the  $i$ th superlattice unit cell. Exemplarily, the obtained Wannier orbitals for a twist-angle of  $\theta = 1.05^\circ$ , which are checked to be exponentially localized, are depicted in Fig. 6.

The transition amplitudes entering the effective superlattice tight-binding model Eq. (3), which are by construction diagonal in valley number, are computed by evaluating

$$t_{i\alpha,j\beta} = N_{SL}^{-1} \sum_{\mathbf{k}\lambda} e^{i\mathbf{k}(\mathbf{A}_i - \mathbf{A}_j)} \mathcal{U}_{\lambda\mathbf{k}}^{(\alpha)\dagger} \epsilon_{\lambda\mathbf{k}} \mathcal{U}_{\lambda\mathbf{k}}^{(\beta)}. \quad (\text{A5})$$

We observe that the amplitude of transition amplitudes drops rather slowly with distance: To recover the weakly dispersing moiré bands of the effective moiré Hamiltonian introduced in Eq. (2), we have to take transition amplitudes between orbitals with a spatial separation of more than 10 superlattice unit cells into account. The single-particle spectrum using transition amplitudes  $\{t_{i\alpha,j\beta}\}$  is depicted in Fig. 7.

## Appendix B: Numerical ground state analysis in the weak coupling limit

The ground state in the weak-coupling regime is obtained by minimizing an energy functional which derives from the mean field Hamiltonian introduced in Eq. (4) where the local mean fields are considered as variational parameters. The computation is conducted on a finite lattice of  $30 \times 30$  superlattice unit cells to capture the rather slowly decaying transition amplitudes  $\{t_{ab}\}$ . Mutually independent mean fields are introduced for a lattice of  $6 \times 6$  superlattice unit cells with imposed periodic boundaries.

The quadratic mean field Hamiltonian is given by (we drop the spin index regarding representation)

$$H_{MF} = \sum_{ab} h_{ab} c_a^\dagger c_b \quad (\text{B1})$$

where the mean field Hamiltonian contains the quadratic part of the effective Hamiltonian Eq. (3) describing free moiré electrons, and mean field terms which are obtained by employing the mean field decoupling introduced in Eq. (6) to the interaction terms of Eq. (3). Eventually,  $h_{ab}$  is represented as hermitian  $d \times d$  matrix where  $d$  represents

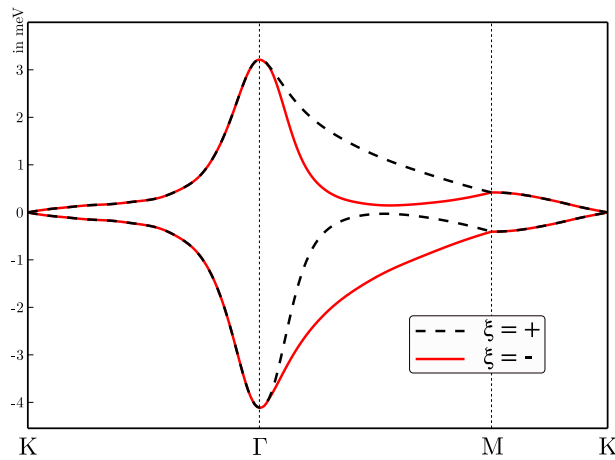


Figure 7. Single-particle spectrum, which is obtained by diagonalizing the effective tight-binding model Eq. (3) for a twist-angle  $\theta = 1.05^\circ$  and  $\alpha = 0.59$ . The dashed-black and red line depict the bands with valley number  $\xi = +$  and  $\xi = -$ , respectively.

the dimensionality of the Hilbert space (in our case  $d = 7200$ ). The energy functional is obtained as the thermal expectation value of the mean field Hamiltonian,

$$E[\langle c^\dagger c \rangle] = Z^{-1} \text{tr}[e^{-H/T} H_{\text{MF}}], \quad (\text{B2})$$

in the limit of zero temperature,  $T \rightarrow 0$ . To evaluate Eq. (B2), correlations of type  $\langle c_a^\dagger c_b \rangle$ , where  $\langle \dots \rangle$  denotes thermal averaging in the limit  $T \rightarrow 0$ , have to be determined self-consistently. We therefore have to compute, given an initial mean field configuration  $\langle c^\dagger c \rangle$ , the single-particle Green's function

$$G_{ab}^{R/A}(\omega) = [\omega - h \pm i0^+]_{ab}^{-1}, \quad (\text{B3})$$

as correlations are given by

$$\langle c_a^\dagger c_b \rangle = i \int_{-\infty}^{\mu} \frac{d\omega}{2\pi} [G_{ab}^R(\omega) - G_{ab}^A(\omega)]. \quad (\text{B4})$$

Determining the inverse of a large matrix is very costly. To overcome this difficulty, we locally approximate the matrix inversion around a certain state  $a$  employing the Lanczos algorithm [49]. This approximation procedure is applicable because  $h$  possesses a local structure, i.e. state  $a$  is locally coupled to only a handful of other states  $b$ . The dimensionality of the Lanczos space  $d_L$ , which is necessary to accurately approximate  $G_{ab}^{R/A}(\omega)$ , is therefore much smaller than the original Hilbert space dimensionality  $d \gg d_L$ . Good results are here obtained for  $d_L = 50$ . To approximate  $G_{ab}^{R/A}(\omega)$ , we construct the Lanczos space around an initial state  $a$ . The transformation is given by a  $d \times d_L$  unitary matrix  $u$  with  $u_{i1} = \delta_{ia}$ , which is provided by the Lanczos algorithm [50], such that  $\tilde{h} = u^\dagger h u$  represents a tridiagonal hermitian matrix. Because of its tridiagonal form and its reduced rank, the propagator in Lanczos space is readily determined exactly to  $\tilde{G}^{R/A}(\omega) = [\omega - \tilde{h} \pm i0^+]^{-1}$  and the single-particle Green's function is eventually given by

$$G_{ab}^{R/A}(\omega) \approx [u \tilde{G}^{R/A}(\omega) u^\dagger]_{ab}. \quad (\text{B5})$$

If the initial mean fields  $\langle c^\dagger c \rangle$  obey Eq. (B4), we obtained a good approximation for the ground state mean field configuration and, by employing Eq. (B2), the corresponding ground state energy.

### Appendix C: Mean field theory of charge-density wave order

In what follows, the mean field theory of the charge density wave order discussed as ground state candidate of the weak-coupling regime in Subsec. II A is specified. The order breaks rotational and translational symmetry specified by the order parameter  $\Delta_{\mathbf{Q}}$  with the ordering vector  $\mathbf{Q}$  given in Eq. (8), but preserves spin and valley symmetry. Thus, only direct interaction channels including on-site, nearest neighbor- (NN), next-to-nearest neighbor- (NNN) and

next-to-next-to-nearest neighbor (NNNN) interactions as discussed in Subsec. **IB** contribute to a possible formation of this particular order. Two aspect will be discussed in the following: The effective interaction strength in the charge density wave channel  $U_{\text{CDW}}$  and the corresponding susceptibility  $\chi_{\mathbf{Q}}$ . Both enter the usual criterion for the onset of order in mean field theories (see e.g. Ref. [51]),

$$1 + [U_{\text{CDW}}\chi_{\mathbf{Q}}^{(0)}(\mu)]|_{\text{cr}} = 0, \quad (\text{C1})$$

which determines a critical interaction strength or doping level.

We start with the interaction part of the effective Hamiltonian Eq. (3) where only direct channels are considered,

$$H_{\text{int}} = \frac{1}{2} \sum_{ab} \sum_{\sigma\sigma'} U_{ab} c_{a\sigma}^\dagger c_{a\sigma} c_{b\sigma'}^\dagger c_{b\sigma'}, \quad (\text{C2})$$

where  $a = (i, \alpha, \xi)$  are the unit cell index  $i$ , basis index  $\alpha \in \{A, B\}$  and valley index  $\xi \in \{+, -\}$ , and the spin index  $\sigma$ . To determine the effective interaction strength, Eq. (C2) is expressed in momentum space by using  $c_{\mathbf{k}\alpha} = \frac{1}{\sqrt{N}} \sum_i e^{i\mathbf{R}_i \cdot \mathbf{k}} c_{i\alpha}$ , where the valley and spin index is dropped for convenience but restored if necessary. By using  $U_{ab} = \sum_i U_i \sum_j \delta_{\mathbf{R}_a - \mathbf{R}_b, \mathbf{A}_j^{(i)}}$  where  $\{\mathbf{A}_j^{(i)}\}$  denotes the set of space vectors connecting the interacting lattice sites for density interactions of type  $i \in \{\text{on-site, NN, NNN, NNNN}\}$ , we obtain

$$H_{\text{int}}^{(i)} = \frac{U_i}{2N} \sum_{\alpha\beta} \sum_{\mathbf{q}} \gamma_{\alpha\beta}^{(i)}(\mathbf{q}) \rho_{\alpha}(\mathbf{q}) \rho_{\beta}(-\mathbf{q}), \quad (\text{C3})$$

where the density operator is given by  $\rho_{\alpha}(\mathbf{q}) = \sum_{\xi\sigma} \rho_{\alpha\xi\sigma}(\mathbf{q})$  with  $\rho_{\alpha\xi\sigma}(\mathbf{q}) = \sum_{\mathbf{k}} c_{\mathbf{k}+\mathbf{q}\alpha\xi\sigma}^\dagger c_{\mathbf{k}\alpha\xi\sigma}$  and the vertex function  $\gamma_{\alpha\beta}^{(i)}(\mathbf{q}) = \sum_j e^{i\mathbf{A}_j^{(i)} \cdot \mathbf{q}}$ , which obeys  $[\gamma_{\alpha\beta}^{(i)}(\mathbf{q})]^* = \gamma_{\beta\alpha}^{(i)}(\mathbf{q}) = \gamma_{\alpha\beta}^{(i)}(-\mathbf{q})$ . For long-range interactions, the vertex functions are determined to

$$\gamma_{AB}^{(\text{NN})}(\mathbf{q}) = e^{-i\mathbf{u}_{AB} \cdot \mathbf{q}} (1 + e^{i\mathbf{q} \cdot \mathbf{A}_1} + e^{i\mathbf{q} \cdot \mathbf{A}_2}), \quad (\text{C4a})$$

$$\gamma_{\alpha\alpha}^{(\text{NNN})}(\mathbf{q}) = 2\{\cos[\mathbf{q} \cdot \mathbf{A}_1] + \cos[\mathbf{q} \cdot \mathbf{A}_2] + \cos[\mathbf{q} \cdot (\mathbf{A}_1 + \mathbf{A}_2)]\}, \quad (\text{C4b})$$

$$\gamma_{AB}^{(\text{NNNN})}(\mathbf{q}) = e^{-i\mathbf{u}_{AB} \cdot \mathbf{q}} [e^{i\mathbf{q} \cdot (\mathbf{A}_1 + \mathbf{A}_2)} + e^{i\mathbf{q} \cdot (\mathbf{A}_1 - \mathbf{A}_2)} + e^{-i\mathbf{q} \cdot (\mathbf{A}_1 - \mathbf{A}_2)}], \quad (\text{C4c})$$

with Bravais lattice vector  $\mathbf{A}_i$  and basis vector  $\mathbf{u}_{AB}$  which connects the crystalline basis sites. For transferred momenta  $\mathbf{Q} \in \{\mathbf{G}_1/2, \mathbf{G}_2/2, (\mathbf{G}_1 + \mathbf{G}_2)/2\}$ , the interaction part reduces to

$$H_{\text{int}} = \frac{1}{N} U_{\text{on-site}} \left[ \sum_{\alpha\xi} \rho_{\alpha\uparrow\xi}(\mathbf{Q}) \rho_{\alpha\downarrow\xi}(\mathbf{Q}) + \sum_{\alpha\sigma} \rho_{\alpha\sigma+}(\mathbf{Q}) \rho_{\alpha\sigma-}(\mathbf{Q}) \right] + \frac{1}{2N} [U_{\text{NN}} - 3U_{\text{NNNN}}] \rho_A(\mathbf{Q}) \rho_B(\mathbf{Q}) - U_{\text{NNN}} \sum_{\alpha} \rho_{\alpha}(\mathbf{Q}) \rho_{\alpha}(\mathbf{Q}), \quad (\text{C5})$$

where the on-site interaction entered with a constant vertex function. Due to the finite momentum transfer, we find negative interaction amplitudes for direct interactions of NNN- and NNNN-type. This is traced back to the fact that for a developed charge density wave order with ordering vector  $\mathbf{Q}$ , interaction contributions from these types of interactions are minimized which can be inferred from the representation of a possible order depicted in Fig. 4. Indeed,  $\gamma_{\alpha\alpha}^{(\text{NNN})}(\mathbf{q})$  and  $\gamma_{AB}^{(\text{NNNN})}(\mathbf{q})$  are minimal and negative for  $\mathbf{q} = \mathbf{Q}$ . Thus, matrix elements  $U_{\text{NNN}}$  and  $U_{\text{NNNN}}$  favor the CDW order with ordering vector  $\mathbf{Q}$ , whereas  $U_{\text{on-site}}$  and  $U_{\text{NN}}$  act against it.

The mean field Hamiltonian is obtained by introducing mean fields  $\langle \rho_{\alpha\sigma\xi}(\mathbf{Q}) \rangle = \Delta_{\mathbf{Q}}/8$  and dropping constant terms yielding

$$H_{\text{MF}} = H_0 + \frac{\Delta_{\mathbf{Q}}}{4N} U_{\text{CDW}} \sum_{\alpha} \rho_{\alpha}(\mathbf{Q}), \quad (\text{C6})$$

where  $H_0$  denotes the quadratic part of Eq. (3) and the effective interaction strength in the charge density wave channel is given by

$$U_{\text{CDW}} = U_{\text{on-site}} + U_{\text{NN}} - 4U_{\text{NNN}} - 3U_{\text{NNNN}}. \quad (\text{C7})$$

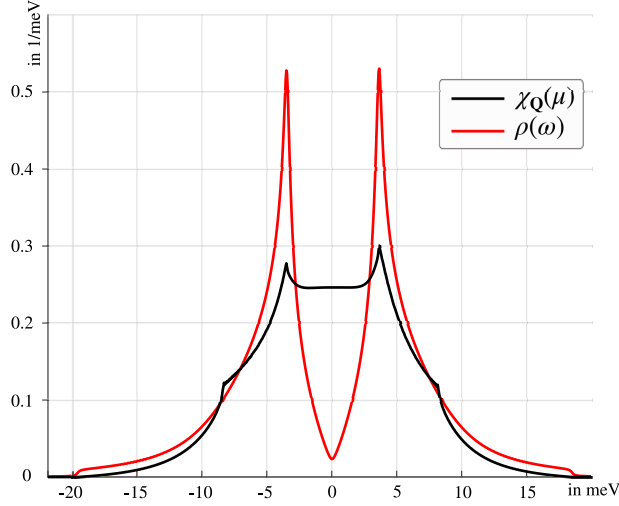


Figure 8. Charge susceptibility (black line)  $\chi_{\mathbf{Q}}(\mu)$  and single-particle density of states (red line)  $\rho(\omega) = -\frac{1}{\pi N} \sum_{\mathbf{k}} \text{Im} G_0^R(\omega, \mathbf{k})$  as function of doping level and frequency, respectively, for a twist-angle representative for the weak-coupling regime.  $\chi_{\mathbf{Q}}$  is slightly peaked at the positions of van Hove points (see the density of states in comparison), but has also finite weight at charge neutrality which is traced back to the finite momentum transfer  $\mathbf{Q}$  lying at the boundaries of the moiré Brillouin zone.

The effective interaction strength is complemented by the charge susceptibility with finite momentum and zero frequency transfer entering the criterion Eq. (C1). By means of standard methods (see e.g. Ref. [51]), it is determined to

$$\chi_{\mathbf{Q}}^{(0)}(\mu) = -\frac{i}{4N} \sum_{\mathbf{k}} \int_{-\infty}^{\mu} \frac{d\omega}{2\pi} \text{tr}_{\alpha\xi\sigma} [G_{\mathbf{k}}^R(\omega) V G_{\mathbf{k}+\mathbf{Q}}^R(\omega) - G_{\mathbf{k}}^A(\omega) V G_{\mathbf{k}+\mathbf{Q}}^A(\omega)], \quad (\text{C8})$$

where the free electronic Green's function is given by

$$G_{0,\alpha\beta}^R(\omega, \mathbf{k}) = ([\omega - h_0(\mathbf{k}) + i0^+]^{-1})_{\alpha\beta}, \quad (\text{C9})$$

with  $h_0$  obtained from the quadratic part of Eq. (3) by Fourier transform being diagonal in spin and valley space, and the vertex part  $V_{\alpha\beta} = \delta_{\alpha,\beta}$ .

The charge susceptibility  $\chi_{\mathbf{Q}}$  is determined as function of doping level  $\mu$  and is depicted in Fig. 8. It is slightly peaked at the positions of van Hove points but does not diverge for any doping level because of the absence of nesting conditions connected with momentum transfer  $\mathbf{Q}$ . Substantial weight is also observed at charge neutrality because of the finite momentum transfer. Combined with an finite attractive interaction  $U_{\text{CDW}} < 0$  whose critical value is determined by Eq. (C1), an onset of charge density wave order is expected for doping levels centered around charge neutrality as depicted in Fig. 2.